ACS APPLIED MATERIALS & INTERFACES

Research Article

www.acsami.org

Direct Electrochemical Synthesis of Reduced Graphene Oxide (rGO)/Copper Composite Films and Their Electrical/Electroactive Properties

Guoxin Xie,*[,†,‡] Mattias Forslund,[†] and Jinshan Pan[†]

[†]Division of Surface and Corrosion Science, Department of Chemistry, KTH Royal Institute of Technology, SE-100 44 Stockholm, Sweden

[‡]State Key Laboratory of Tribology, Department of Mechanical Engineering, Tsinghua University, Beijing 100084, China

ABSTRACT: Electrical contact materials with excellent performances are crucial for the development and safe use of electrical contacts in different applications. In our work, reduced graphene oxide (rGO)/copper (Cu) composite films, as potential electrical contact materials, have been synthesized on copper foil with one-step electrochemical reduction deposition method. Cyclic voltammetry (CV) was used to define the deposition conditions, and confocal Raman microscopy (CRM), X-ray photoelectron spectroscopy (XPS) and scanning electron microscopy (SEM) were used to characterize the chemical compositions, molecular and micro- and nano-structures of the composite films. Atomic force microscopy/scanning Kelvin probe force microscopy (AFM/SKPFM), conductive AFM (C-AFM) as well as impedance analysis were employed to evaluate the electroactive/electrical properties of the prepared composite films, respectively. The CRM and XPS results suggest that the rGO/Cu composite films can be synthesized through one-step electrochemical codeposition using suitable precursor solutions. Within a short deposition period, the growth of discrete nanograins in the composite film predominates, whereas pine-tree-leaf nanostructures are formed in the composite film when the deposition period is long, due to the chelating role of GO or rGO to regulate the growth rate of metallic copper nanograins. The electrical resistivity of the composite films is lower than the polished Cu foil and the electrodeposited Cu film, probably due to the higher conductivity (enhanced transfer of charge carriers) of the rGO incorporated in the composite films. The Volta potential variation in the rGO/Cu composite film is quite different from that in the electrodeposited Cu film. The electroactivity of the rGO/Cu composite films is higher than the electrodeposited Cu film, but lower than polished Cu foil, and the underlying mechanisms have been discussed.

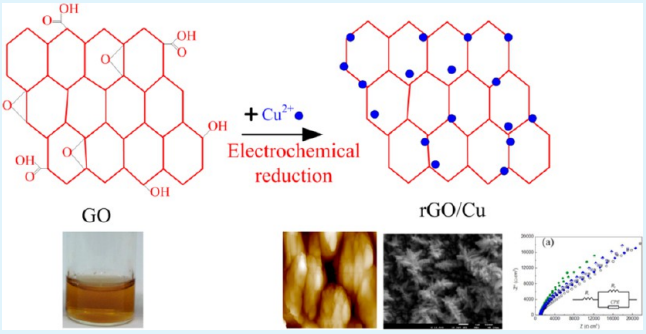

KEYWORDS: *rGO/Cu composite film, electrochemical synthesis, electrical contact material, electrical/electroactive properties*

1. INTRODUCTION

Development of novel materials with excellent mechanical and electrical as well as corrosion resistance properties are of great importance for high efficiency and reliability of future electrical contacts.[1] Traditionally, materials used for electrical contact surfaces are mostly transition metals, e.g., gold (Au), silver (Ag) and copper (Cu) as well as their alloys and composites.[2−6] Usually, compromises between low contact resistance, good mechanical/tribological properties, stability and cost are necessary. For instance, these base metals possess high electrical conductivity but low wear resistance, and they may also tarnish or corrode easily during exposure to moisture and airborne contaminants.[1] Incorporation of graphite, molybdenum disulfide (MoS_2) and nickel (Ni), etc., into these matrix metals improves the tribological properties but sacrifices the electrical conductivity and corrosion resistance.[6−8] Extensive efforts have been made in the past decade seeking for better solutions. For example, self-lubricating transition metal (carbide or nitride)-based composite hard coatings have been developed by sputtering.[9−11] Also, conductive solid lubricant layers on top of electrical contact substrates have been utilized for improving the tribological properties while maintaining good electrical conductivity. Typically, silver iodide (AgI) coatings have been electrodeposited on Ag-plated Cu coupons as the solid lubricant for sliding electrical contacts.[12] Moreover, different allotropes of carbon also have been used as the outermost layers in between electrical contact pairs. Graphitized carbon interfacial layer transformed from amorphous carbon films, or carbon-60 films deposited between Ni film and silicon carbide (SiC), could affect the specific electrical contact resistance.[13,14] A porous carbon electrode made of activated carbon powder with carbon black conductive additives was cemented by a polymer binder onto a metal current collector to reduce interfacial electrical resistance.[15] Carbon nanotube layers as the interfacial material were demonstrated to reduce the contact resistance of Cu/Cu interfaces,[16] and believed to be appropriate

Received: February 10, 2014
Accepted: April 21, 2014
Published: May 1, 2014

substitutes of conventional carbon-based or solid metal "brushes" for sliding/rotating electrical contacts.[17]

Graphene emerged recently as a very attractive material that possesses excellent electrical[18,19] and thermal conductivities,[20] and good mechanical and tribological[21,22] as well as corrosion resistance properties.[23−25] Different graphene-based metal or metal oxide composite films have been synthesized for electrical contact/electrode materials,[26−36] biosensing[37,38] or electrocatalytic purposes,[39,40] due to the increases of the film's conductivity or specific surface area after incorporating graphene. The synthesis methods include simple solution method,[26] chemical vapor deposition and layer-by-layer deposition technique,[41] chemical or electrochemical post-reduction of pre-deposited coatings,[27−31,37,39,40] as well as electrochemical codeposition of metal precursor and graphene oxide (GO) sheets,[32−36,38] etc. In the latter case, the dispersibility of GO sheets and positively-charged metal ions in the one-pot aqueous precursor solution could affect the co-deposition efficiency, because of the presence of abundant negatively charged functional groups (e.g., ionized carboxyl and phenolic hydroxyl groups) on the GO sheet surfaces.[42] Despite the challenge, the one-step electrochemical codeposition of GO and metal ion precursors without further treatments is a very attractive method for deposition of the composite films because it could simplify the synthesis process and reduce the cost and is suitable for mass production of controllable and conformal films without the need of volatile solvents or reducing agents.[43] Nevertheless, few studies have been devoted to the synthesis of reduced graphene oxide (rGO)/metal composite by the one-step electrodeposition method.[33,34,44] Hence, further efforts to explore the synthesis process of rGO/metal composite films and to understand the relationship between the microstructure and the film's performance are of great value from both scientific and engineering viewpoints. In the present work, rGO/Cu composite films were synthesized on polished copper foil with a one-step electrochemical codeposition method, and the film structure and electrical/electroactive properties were characterized by using various analytical techniques.

2. EXPERIMENTAL SECTION

2.1. Material, Preparation and Characterization. Aqueous suspension of GO sheets (5 mg·mL^{-1}) was purchased from Angstrom Materials Inc., OH, U.S.A., with X and Y dimension around 500 nm and Z dimension 1.0−1.2 nm, 46 wt % carbon and 46 wt % oxygen according to specifications. Pure water (18.2 MΩ·cm) used in this work was obtained from a Milli-Q integral water purification system. Cu foils were purchased from Alfa Aesar (1.0 mm thick, 99.99 % purity), and copper sulfate ($CuSO_4$, >99 %) from Merck Millipore. The Cu foils were carefully polished with grinding papers (from grid 500 to 4000) and subsequently with diamond paste (diameter: 1 μm) to obtain a mirror finish surface. The polished foils were ultrasonically rinsed with ethanol and water thoroughly, followed by drying under a nitrogen stream, and used immediately for electrodeposition.

$CuSO_4$ solutions with the concentrations ranging from 0.05 to 0.005 M, and GO aqueous solutions (concentrations: 0.1 and 0.5 mg·mL^{-1}) were prepared. These two kinds of aqueous solutions were mixed together in equal volumes. The pH values of the mixture solutions were determined by using pH test strips (0.1 to 14 pH range, Whatman). The ionic conductivity of the prepared suspensions was measured by the ac impedance method in an electrochemical cell with a two-platinum-electrodes setup, and the frequency ranged from 1 Hz to 100 kHz with perturbation amplitude of 10 mV. As calibration, measurements using a KCl standard solution of known concentration and conductivity were performed to determine the cell constants.

2.2. Synthesis and Characterization of rGO/Cu Composite Films. The electrochemical experiments were performed by using an Autolab instrument (Metrohm Autolab B. V. Netherlands), and a three-electrode electrochemical cell with the sample as working electrode, a saturated Ag/AgCl electrode as reference electrode, and a Pt mesh as counter electrode. In this paper, all the potential values are given versus the saturated Ag/AgCl reference electrode. Cyclic voltammetry (CV) experiments of the precursor mixture solutions of 8 mL were performed, the potential was swept in the range of +0.8 V to −1.4 V with a sweep rate of 20 mV·s^{-1}, and commenced initially at +0.6 V to the cathodic direction. The working electrode for the CV experiments was a Pt foil polished with 4000 grid grinding paper and 1 μm diamond paste. After that, constant potential deposition experiments using the Cu foils as working electrodes were performed by applying different cathodic potentials (chosen on the basis of the CV curves) for various deposition times with magnetic stirring and nitrogen bubbling.

The prepared composite films were characterized with confocal Raman microscopy (CRM), X-ray photoelectron spectroscopy (XPS), scanning electron microscopy (SEM) and atomic force microscopy/scanning Kelvin probe force microscopy (AFM/SKPFM). The CRM analyses were conducted by using a WITec alpha 300 system equipped with a Nikon NA0.9 NGC objective with 100× magnification and a pinhole of 50 μm in diameter. The samples were excited with a 785 nm red laser; the lateral resolution was 320 nm, and the vertical resolution was around 2 μm.[45] The XPS measurements were carried out by using a PHI Quantera spectrometer with a monochomatic Al Kα X-ray source (26 W) in high vacuum (1×10^{-9} Torr). The analysis area was 300 × 300 μm, and the detected depth was up to 5 nm. The main core level photoemission spectra of Cu, O and C, as well as the X-ray excited Auger spectra of copper (Cu LMM) were taken (energy increment: 0.1 eV). For all the spectra, the binding energy was calibrated with the C 1s peak position (284.8 eV). The data was post-processed with the XPSPEAK software program. The SEM examination was conducted by using a JEOL-7001 SEM with a field emission gun (FEG), and the acceleration voltage of the electron beam was 20 kV. The AFM/SKPFM experiments were carried out with an Agilent 5500 AFM, and both the topographic and corresponding Volta potential images were obtained simultaneously. Dynamic mode with a single-pass methodology was used in the Volta potential mapping using SCM-PIT probes from Bruker Corporation. The physical concept of the Volta potential is closely related to the work function of the metal, i.e. the energy required to pull an electron from the Fermi level of a metal to vacuum. In the SKPFM measurement, a vibrating scanning tip and "nulling" technique were used, and the Volta potential obtained was actually the local relative potential difference versus the tip.[46] For metal surfaces, higher Volta potential corresponds to higher relative nobility. The electrical conductivity mapping of the prepared films was also performed with a conductive AFM (C-AFM) instrument (Asylum Research MFP-3D) under the contact mode. A Ti/Ir coated probe (ASYELEC-01) with a nominal spring constant of 2 N/m was employed, and the applied load was approximately 290 nN and the scan rate 1 Hz.

The electrical resistivity of the prepared composite films was measured with a Solartron SI 1260 impedance/Gain-phase analyzer, with a sample holder consisting of two circular parallel gold electrodes. The sample was fixed in between the two electrodes and pressed tightly through adjusting the screws at the corners of the holder, and the contacting force in the experiments was kept as close as possible. Since the two gold electrodes and the sample were under planar parallel contact, the contact pressure would not vary so dramatically as that in the point contact case when the contact force changes slightly. Electrochemical impedance spectroscopy (EIS) measurements of the prepared composite films were performed in 0.01 M NaCl solution, using the Autolab instrument. The EIS measurements were performed at the open-circuit potential (OCP) with a perturbation amplitude of 10 mV and the frequency range from 10^5 down to 4×10^{-3} Hz. All the measurements were performed at room temperature and repeated at least three times.

Table 1. Ingredients of the Precursor Solutions and Their pH Values and Electrical Conductivities

sample number	ingredient	pH value	electrical conductivity ($mS \cdot cm^{-1}$)
1	Cu^{2+} 0.01 M	4.5	2.33
2	Cu^{2+} 0.05 M/GO 0.5 $mg \cdot mL^{-1}$	4.0−4.5	4.43
3	Cu^{2+} 0.04 M/GO 0.5 $mg \cdot mL^{-1}$	4.0−4.5	3.70
4	Cu^{2+} 0.03 M/GO 0.5 $mg \cdot mL^{-1}$	4.5−5.0	3.11
5	Cu^{2+} 0.02 M/GO 0.5 $mg \cdot mL^{-1}$	5.0−5.5	2.19
6	Cu^{2+} 0.01 M/GO 0.5 $mg \cdot mL^{-1}$	~5.5	1.53
7	Cu^{2+} 0.005 M/GO 0.5 $mg \cdot mL^{-1}$	~5.5	0.92
8	Cu^{2+} 0.01 M/GO 0.1 $mg \cdot mL^{-1}$	~5.5	1.27

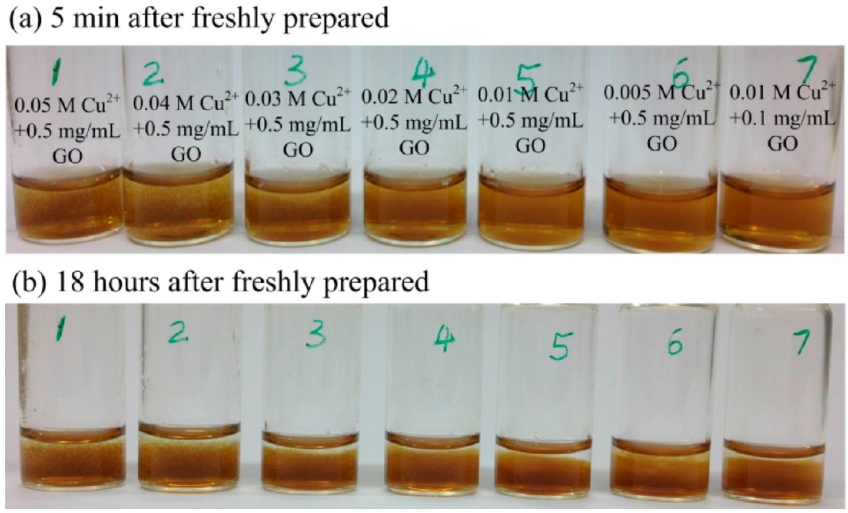

Figure 1. Photos of the prepared precursor solutions: (a) 5 min after fresh preparation; (b) 18 h after fresh preparation.

3. RESULTS AND DISCUSSION

3.1. Stability of Precursor Solutions. The basic ingredients in the precursor solutions investigated and the electrical conductivity as well as the pH value of the solutions are shown in Table 1. The photos of these precursor solutions are shown in Figure 1. It can be seen that, the pH values of these solutions are in the range of 4.0−5.5, which is higher than the point of zero charge (pH_{pzc}) value of GO (around 3.8),[47] indicating negatively charged surfaces of the GO sheets. Therefore, the addition of positively charged Cu^{2+} ions would easily interact electrostatically with the negatively charged groups on the GO surface. High concentrations of Cu^{2+} ions would decrease the separation between Cu^{2+} ions and charged GO sheets, resulting in an increased electrostatic attraction between the opposite charges and formation of agglomerates. As shown in Figure 1a, minor agglomerates are obviously present in the Cu^{2+} 0.05 M/GO 0.5 $mg \cdot mL^{-1}$ solution. The solution becomes increasingly clearer after gradually reducing the relative ratio of Cu^{2+} to GO at a fixed GO concentration; meanwhile the solution conductivity decreases correspondingly (Table 1). At low Cu^{2+} concentrations (0.01 and 0.005 M), the solutions appear to be transparent, and no obvious precipitation can be seen in the solutions after 18 h storage, Figure 1b. It follows that a further decrease of the GO concentration would be favorable for the good dispersion of the precursor solution. On the other hand, a low electrical conductivity of the solution would negatively affect the electron transfer efficiency in the electrochemical deposition process. On the basis of these considerations, the solutions of Cu^{2+} 0.01 M/GO 0.5 $mg \cdot mL^{-1}$ and Cu^{2+} 0.01 M/GO 0.1 $mg \cdot mL^{-1}$ were chosen for detailed investigations in this study.

3.2. CV Measurements. Cyclic voltammograms of Cu^{2+} 0.01 M and Cu^{2+} 0.01 M/GO 0.5 $mg \cdot mL^{-1}$ solutions are given in Figure 2. In the case of the Cu^{2+}/GO solution, the curves

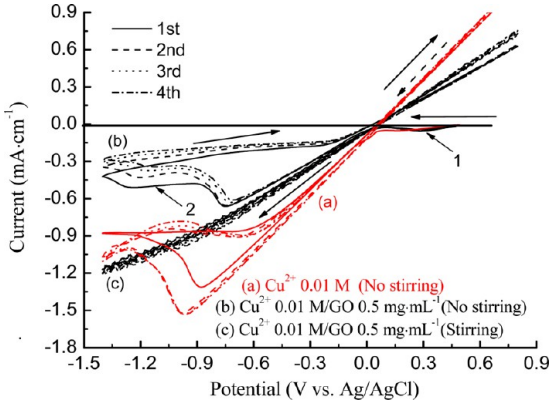

Figure 2. CV curves of (a) Cu^{2+} 0.01 M solution without stirring, Cu^{2+} 0.01 M/GO 0.5 $mg \cdot mL^{-1}$ solution (b) without stirring and (c) with stirring.

obtained without and with magnetic stirring were included for comparison. For the Cu^{2+} solution, curve (a), the cathodic current begins to emerge in the first cycle after the potential was decreased to +0.5 V (Arrow 1), corresponding to the onset of underpotential deposition of Cu onto the Pt substrate.[48] After the potential is swept more negative than +0.1 V, overpotential bulk deposition of Cu starts,[49] evidenced by the steep increase of the cathodic current with the decreasing potential, which reaches a diffusion-controlled peak around the

dx.doi.org/10.1021/am500768g | ACS Appl. Mater. Interfaces 2014, 6, 7444−7455

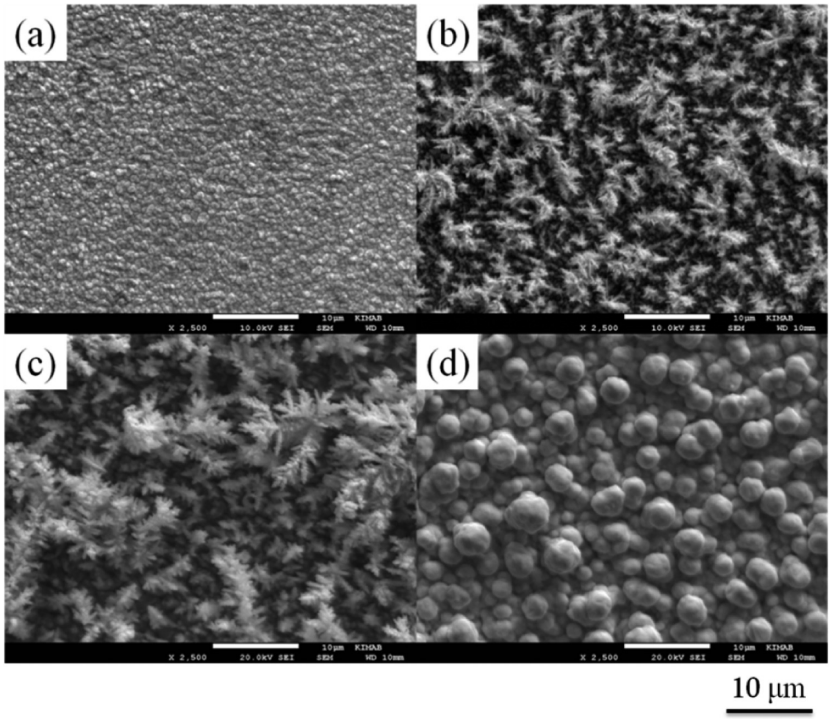

Figure 3. SEM morphologies of Cu^{2+} 0.01 M/GO 0.5 mg·mL^{-1} solutions deposited under −1.2 V at different deposition times: (a) 10 min; (b) 30 min; (c) 60 min, and (d) under −0.4 V for 180 min.

potential of −0.9 V. After the reversal of potential sweep at -1.4 V, the cathodic current decreases gradually and later the current becomes positive. Further sweep in the anodic direction would increase the anodic current due to the dissolution of the just deposited Cu film. During the subsequent scans, the cathodic peaks are almost same, whereas their peak potentials are more negative than that in the first cycle due to the higher ionic concentration near the electrode surface after the first deposition/dissolution cycle. When the GO is added, i.e., in the Cu^{2+}/GO solution without stirring, curve (b), both the cathodic and the anodic currents are lower than those in the Cu^{2+} solution due to fewer Cu ions deposited/dissolved on the substrate. Besides, another minor peak emerges at the potential of around −1.1 V in the cathodic scan in the Cu^{2+}/GO solution (Arrow 2), and such a peak typically originates from the irreversible electrochemical reduction of oxygen functional groups on the GO surface.[50,51] The cathodic current under the diffusion control decreases slightly in the Cu^{2+}/GO solution as the potential cycling proceeds. In the case of the Cu^{2+}/GO solution with stirring (curve (c)), the cathodic current changes almost linearly without obvious peaks in the potential range investigated. Moreover, the current curves for the four potential cycles are very close to each other and are slightly higher with the increasing cycles, which is probably due to the increase of the effective surface area of reduced GO films.[52]

3.3. Structural and Composition Characterizations. *3.3.1. SEM Morphology.* Figure 3 shows the SEM morphologies of the prepared composite films from the precursor solution of Cu^{2+} 0.01 M/GO 0.5 mg·mL^{-1}. Panels a−c of Figure 3 show the evolution of the film morphology with deposition time under a deposition potential of −1.2 V. As shown in Figure. 3a, after deposition for 10 min, many small spherical particles were formed and uniformly distributed on the film surface, and the particle diameter is around 1 μm, similar to the features of electrodeposited Cu film.[53] After the deposition for 30 min, the film surface exhibits pine-tree-leaf hierarchical nanostructures, with trunks of 100 nm in diameter, Figure 3b. Many branches stretch out from the main trunk, with an average diameter of 50 nm and a length of 0.5−1 μm. After increasing the deposition time to 60 min, the nanostructures grow larger and denser, as shown in Figure 3c. On the other hand, when the deposition potential was −0.4 V, the pine-tree-leaf nanostructures were not observed after the deposition for 3 h. Instead, many spherical particles were formed, with an average diameter of 2 μm, Figure 3d. The observed pine-tree-leaf nanostructure of the composite film is very similar to the hierarchical assembly of nanoscale building architectures obtained by using hydrothermal and solvothermal methods.[54] Although pine-tree-leaf hierarchical superstructures of cobalt nanofibers,[55] carbon-coated ferric oxide composites[56] and β-nickel sulfide[57] have been reported recently, these interesting nanostructures have seldom been observed for electrodeposited films with precursor solutions of GO mixed with Cu^{2+} ions.

The formation mechanism of the pine-tree-leaf like rGO/Cu nanostructures synthesized in this work is still not very clear. In analogue to the results previously reported in refs 54.-57, the growth mechanism of the rGO/Cu superstructures could be speculated as follows: Part of Cu^{2+} ions in the solution coordinate with the deprotonated carboxylate anions of GO (GO^-) to form GO−Cu^{2+} complexes. During the deposition, Cu^{2+}, GO^-, and GO−Cu^{2+} complexes are sufficiently transferred to the region near the Cu substrate surface with the assistance of mechanical stirring. At the early stage of deposition, under a large cathodic potential the Cu^{2+} ions and GO−Cu^{2+} complex are preferably reduced/deposited onto the active sites of the substrate surface to form regular and evenly-distributed nuclei. And, more GO^- or GO−Cu^{2+} complexes will be reduced/deposited on the formed nuclei after a long duration, leading to the growth of regular spherical

particles. As a result, spherical particles will tend to link together to form a one-dimensional main trunk, and subsequently new nucleation would start on the active sites on the trunk surface, resulting in the branch growth. Apparently, GO or rGO plays an important role in chelating Cu^{2+} ions and regulating the reaction rate of generating metallic Cu to promote the growth of pine-tree-leaf nanostructures.[55]

3.2. CRM and XPS Analyses. The chemical structural and composition as well as the chemical state of the surface species of the prepared rGO/Cu composite films were analyzed by using CRM and XPS techniques. Figure 4 shows the Raman

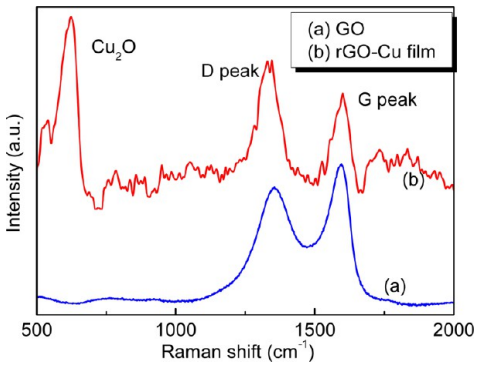

Figure 4. Raman spectra of (a) the GO precursor and (b) prepared composite film [precursor: Cu^{2+} 0.01 M/GO 0.5 mg·mL^{-1}, deposition condition: −1.2 V and 60 min].

spectra of the GO precursor and the deposited rGO/Cu composite film obtained from a precursor solution of Cu^{2+} 0.01 M/GO 0.5 mg·mL^{-1} under −1.2 V for 60 min, respectively. Two major peaks at 1330−1360 cm^{-1} and 1590−1600 cm^{-1} are present in the two spectra, which are normally referred to as D and G bands, respectively.[58] The D band associates with the A_{1g} mode, which mainly arises from disorders and edges in graphite materials, while the G band corresponds to the symmetric E_{2g} mode, which originates from in-plane sp^2 carbon−carbon double bond stretching motion.[59] The presence of D and G bands on the spectra of the composite film suggests the GO precursor has been deposited on the Cu substrate. Moreover, the intensity ratio between D and G bands (I_D/I_G) increases dramatically after the GO precursor was electrochemically reduced and deposited in the composite film. This phenomenon is primarily due to the formation of new domains of conjugated carbon atoms as well as the increase of defect density,[33,39,60,61] indicating partial reduction of the GO precursor. Another two peaks at around 525 and 627 cm^{-1} are the characteristic peaks of cuprous oxide (Cu_2O),[62] which could be formed on the metallic copper surface in air after termination of the deposition (the shortest period in air before the Raman analyses was about 24 h). These Raman spectra provide evidence for the electrochemical reduction of Cu^{2+} ions and GO, and formation of rGO and Cu in the deposited composite film.

Moreover, the distribution of the rGO and Cu domains in the composite film was investigated by using the CRM mapping, and the results are shown in Figure 5. The domains with bright Cu_2O signal most likely are Cu domains in the film since Cu_2O is formed on metallic Cu. And, a good correlation between the bright D and G signals suggests that these sites are rGO domains (with high I_D/I_G ratio). For the rGO/Cu composite films deposited under −1.2 V for 10 min, Figure 5a, and −0.4 V for 180 min, Figure 5d, the sizes of the domains of Cu (bright Cu_2O signal) and rGO (bright D and G signals) are in the range of 1−2 μm, close to the particle size observed with SEM, Figure 3a,d. When the deposition duration was increased to 30 or 60 min, the distributions of these domains were less uniform, as shown in b and c of Figure 5. This is primarily due to the presence of pine-tree-leaf hierarchical structures, resulting in less uniform elemental distributions, and these hierarchical structures could also affect the focus in the CRM measurements.

Furthermore, the chemical states of different elements present in the rGO/Cu composite films were analyzed by using high-resolution XPS. As an example, Figure 6 displays the detailed XPS spectra of the rGO/Cu composite film deposited from the precursor solution of Cu^{2+} 0.01 M/GO 0.5 mg·mL^{-1} under −1.2 V for 60 min. Figure 6a depicts the C 1s spectrum of the film, where the main peak at 284.8 eV corresponds to the sp^2-bonded carbon, and the small deconvoluted peaks at 286.3, 287.7, and 288.6 eV represent the C−O, C═O and O−C═O bonds, respectively.[38,43] Correspondingly, the O 1s spectrum can be deconvoluted into four peaks: the two peaks with binding energies of 533.4 and 531.8 eV can be assigned to the C−O and C═O/O−C═O bonds;[18,62] the other two peaks with binding energies of 530.6 and 530.9 eV are associated with the Cu_2O and $Cu(OH)_2$,[63,64] respectively. The main peaks in the Cu 2p spectrum at 932.7 eV (Cu $2p_{3/2}$) and 952.7 eV (Cu $2p_{1/2}$) are assigned to the spectral overlap of metallic Cu−Cu bond and Cu_2O, and the peak at 934.3 eV corresponds to $Cu(OH)_2$.[63,64] The strong peak at 570.3 eV in the Cu LMM spectrum further confirms that Cu_2O is abundant on the top surface layer of the composite film.[63] In order to estimate the atomic percentage of rGO in the composite film, the relative atomic concentrations of different carbon bonds were calculated from the corresponding peak areas in the C 1s spectrum, taking into account the sensitivity factors (using XPSPEAK software) and using linear background subtraction. The calculated results are summarized in Table 2. As can be seen, the percentage of the C−C bond (i.e., carbon in reduced form) in the total carbon element is mostly around 85%. Even though some of carbon surface contamination may contribute to the this type of carbon component, the very high percentage of the reduced carbon in the surface layer indicates that the majority of oxygen-containing groups, e.g., carboxyl and hydroxyl groups, on the GO sheet surfaces have been successfully reduced during the electrochemical codeposition of the composite films. The XPS results are in agreement with the Raman results, confirming the formation of rGO/Cu composite film through the one-step electrochemical codeposition process.

3.4. Electrical and Electroactive Properties. *3.4.1. Electrical Resistance Measurement.* The measured electrical resistivity values of the polished Cu foil, electrodeposited Cu film and rGO/Cu composite films are given in Table 3. The electrical resistivity is 35.41 mΩ·m for the polished Cu foil and 38.39 mΩ·m for the deposited Cu film. The slightly higher resistivity of the deposited Cu film is due to oxygen impurity inside the film[35] and native oxide formed on the surface after deposition. The resistivity values of all the rGO/Cu composite films are in the range between 31 and 35 mΩ·m, mostly lower than that of the polished Cu foil, indicating that the rGO sheets as a conducting network contribute to an enhanced flow of charge carriers between the gold electrodes in the measuring setup. If the contacting surfaces are ideally flat, the current

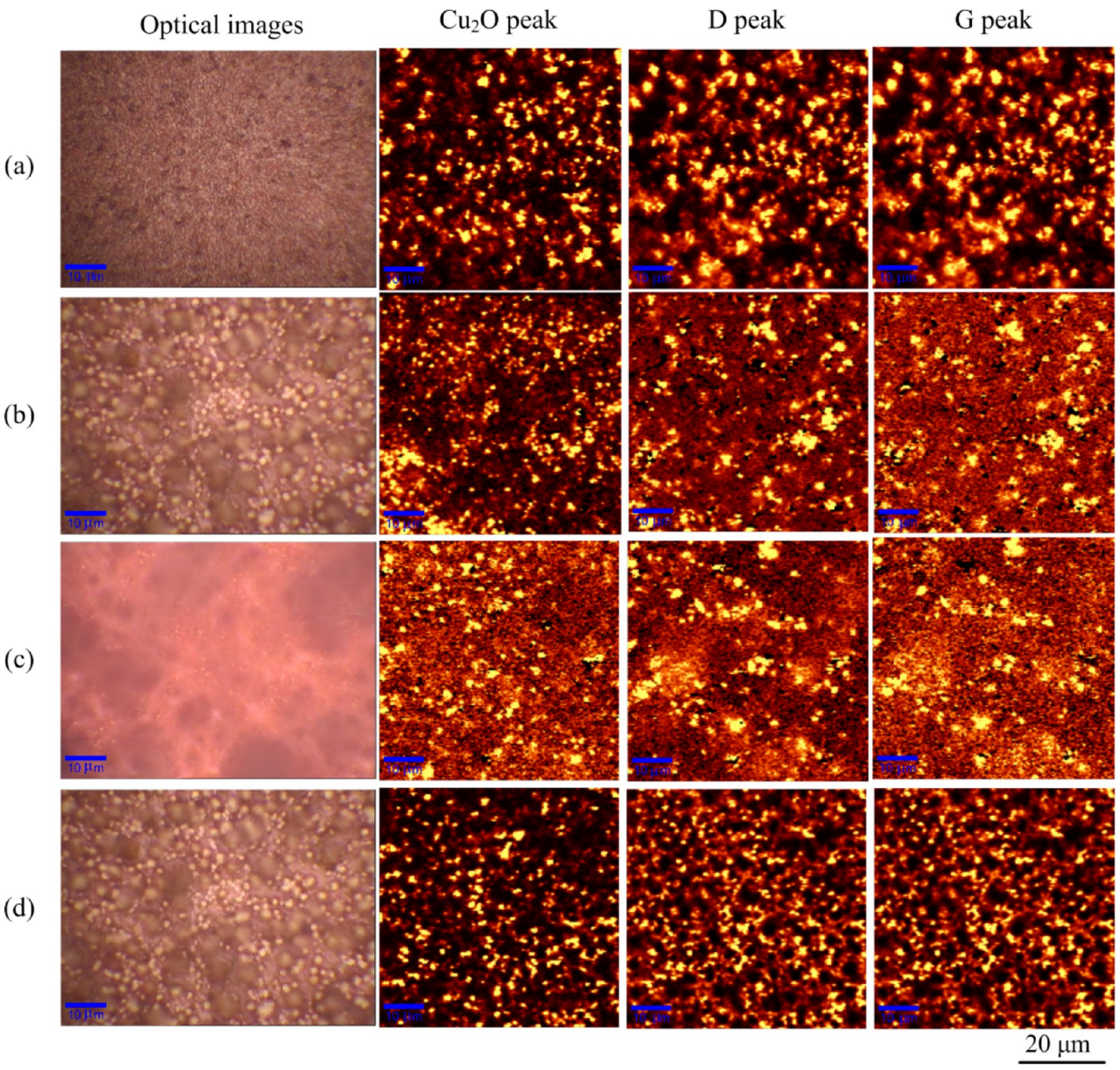

Figure 5. CRM mapping of the rGO/Cu composite films deposited from the precursor solution of Cu^{2+} 0.01 M/GO 0.5 mg·mL^{-1} under different deposition conditions: (a) −1.2 V and 10 min; (b) −1.2 V and 30 min; (c) −1.2 V and 60 min and (d) −0.4 V and 180 min.

passes the contact, and the composite films would preferably flow through the conductive channels where the local resistivity is lower than other parts of the composite film.

As shown in the current mapping by using C-AFM, Figure 7, there are many bright areas in the composite film that exhibit higher local electrical current, Figure 7b, hence higher local electrical conductivity. Under the contact force used in the measurement, the bright areas are estimated to be less than 20% of the total mapping area. Moreover, the current contrast in Figure 7b is not in accordance with the topography contrast in Figure 7a over the same region of the composite film, which suggests that the higher local current is due to the intrinsic higher electrical conductivity of these local areas rather than the signal cross talk with the topography. Most likely these local areas with higher electrical conductivity are domains of the rGO that have higher intrinsic electrical conductivity than the other part of the composite film, i.e., Cu domains (covered by a thin layer of Cu_2O). Furthermore, the real contact area in contact with the gold electrodes in the measuring setup may be significantly smaller than the nominal geometrical area due to the prominent asperities of the deposited composite film,[1] as seen in Figure 3. Thus, the real electrical resistivity of the rough rGO/Cu composite films should be even lower than the measured value.

3.4.2. AFM/SKPFM Observations. From the AFM measurements, concurrent topography and phase images as well as Volta potential maps were obtained for the electrodeposited Cu film, and two rGO/Cu films formed under different potentials and from different precursor solutions. The AFM topographic image in Figure 8a for the electrodeposited Cu film from the $CuSO_4$ 0.01 M solution reveals many small spherical Cu particles of ∼90 nm in diameter. In the phase image in Figure

dx.doi.org/10.1021/am500768g | ACS Appl. Mater. Interfaces 2014, 6, 7444−7455

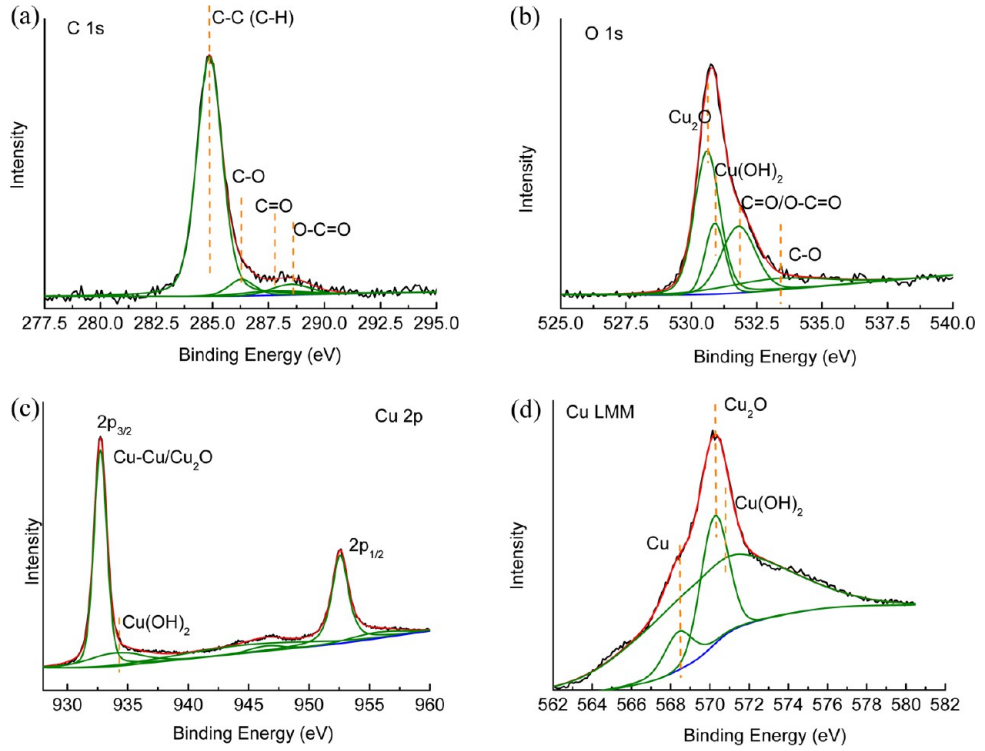

Figure 6. XPS spectra of the rGO/Cu composite film deposited from the precursor solution of Cu^{2+} 0.01 M/GO 0.5 mg·mL^{-1} under −1.2 V for 60 min: (a) C 1s spectrum; (b) O 1s spectrum; (c) Cu 2p spectrum and (d) Cu LMM spectrum.

Table 2. Atomic Percentages of Different Bonds of Carbon Calculated by Fitting the C 1s Spectra of the Deposited Films

	atomic percentage (%)			
sample	C−C (284.8 eV)	C−O (286.3 eV)	C═O (287.8 eV)	O−C═O (288.5 eV)
Cu^{2+} 0.01 M/GO 0.5 mg·mL^{-1} (−1.2 V, 60 min)	85.38	5.96	3.42	5.24
Cu^{2+} 0.01 M/GO 0.5 mg·mL^{-1} (−1.2 V, 20 min)	86.36	4.95	7.67	1.01
Cu^{2+} 0.01 M/GO 0.1 mg·mL^{-1} (−0.8 V, 10 min)	86.31	6.24	5.77	1.68

Table 3. Measured Electrical Resistivities of the Polished Cu Foil, Electrodeposited Cu Film and rGO/Cu Composite Films

sample number	materials	electrical resistivity (mΩ·m)
1	copper	35.41 ± 1.9
2	copper film [Cu^{2+} 0.01 M (−0.8 V 10 min)]	38.39 ± 1.32
3	rGO/Cu film [Cu^{2+} 0.01 M/GO 0.1 mg·mL^{-1}, (−0.8 V, 1 min)]	32.29
4	rGO/Cu film [Cu^{2+} 0.01 M/GO 0.1 mg·mL^{-1}, (−-0.8 V, 5 min)]	32.74
5	rGO/Cu film [Cu^{2+} 0.01 M/GO 0.1 mg·mL^{-1}, (−0.8 V, 10 min)]	30.15
6	rGO/Cu film [Cu^{2+} 0.01 M/GO 0.5 mg·mL^{-1}, (−1.2 V, 20 min)]	31.2 ± 0.35
7	rGO/Cu film [Cu^{2+} 0.01 M/GO 0.5 mg·mL^{-1}, (−1.2 V, 30 min)]	34.76
8	rGO/Cu film [Cu^{2+} 0.01 M/GO 0.5 mg·mL^{-1}, (−1.2 V, 60 min)]	33.91 ± 0.83
9	rGO/Cu film [Cu^{2+} 0.01 M/GO 0.5 mg·mL^{-1}, (−0.8 V, 120 min)]	32.39 ± 1.67
10	rGO/Cu film [Cu^{2+} 0.01 M/GO 0.5 mg·mL^{-1}, (−0.4 V, 180 min)]	32.27

8b, the contrast between the two phases is very obvious, and the many small bright spots correspond to deposited Cu particles homogeneously distributed on the surface. The Volta potential image over the same area in Figure 8c shows the local potential variation, and the Volta potential for the newly formed Cu particles is slightly lower than the surrounding areas. On the surface of the rGO/Cu film deposited from the Cu^{2+} 0.01 M/GO 0.1 mg·mL^{-1} solution under -0.8 V for 10 min, Figure 8d, many quasi-spherical particles are distinguishable on the irregular cluster surfaces. However, the phase image in Figure 8e shows the presence of layered structure of the clusters, which could be the stacked rGO sheets. Moreover, there are less densely distributed particles on the surfaces of the layered structures. Since no clear overlap between the bright spots of the Cu_2O domains and those of the rGO domains in the CRM results, a and d of Figure 5, it is reasonable to speculate that part of the deposited spherical particles shown in Figure 3d are due to the formation of spherical clusters from the rGO sheets, and many small Cu nuclei are formed and attached on these clusters for reaching the surface energy minimum. The continuous dark area in Figure 8f at the boundary of the layered structures suggests the corresponding area has lower nobility. For the rGO/Cu composite film with pine-tree-leaf hierarchical nanostructures, Figure 3b, the AFM topography image in Figure 8g shows elliptical clusters aligned almost in the same direction, with a typical size of 1.3 μm in length and 400 nm in width. The phase image in Figure 8h shows more clearly the layered structure with small particles on the surface. In the Volta potential image, Figure 8i, the Volta

dx.doi.org/10.1021/am500768g | ACS Appl. Mater. Interfaces 2014, 6, 7444−7455

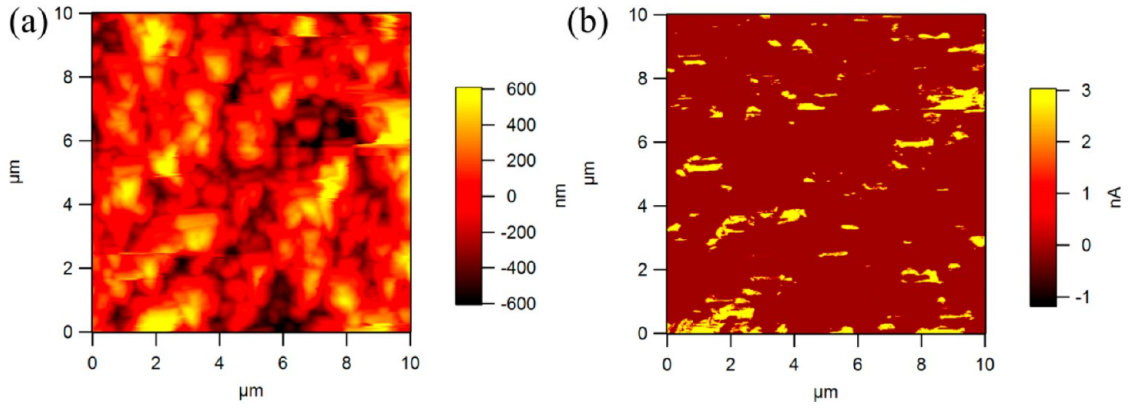

Figure 7. C-AFM current mapping of the rGO/Cu composite film deposited from Cu^{2+} 0.01 M/GO 0.5 mg·mL^{-1} at −1.2 V for 30 min: (a) topography; (b) current.

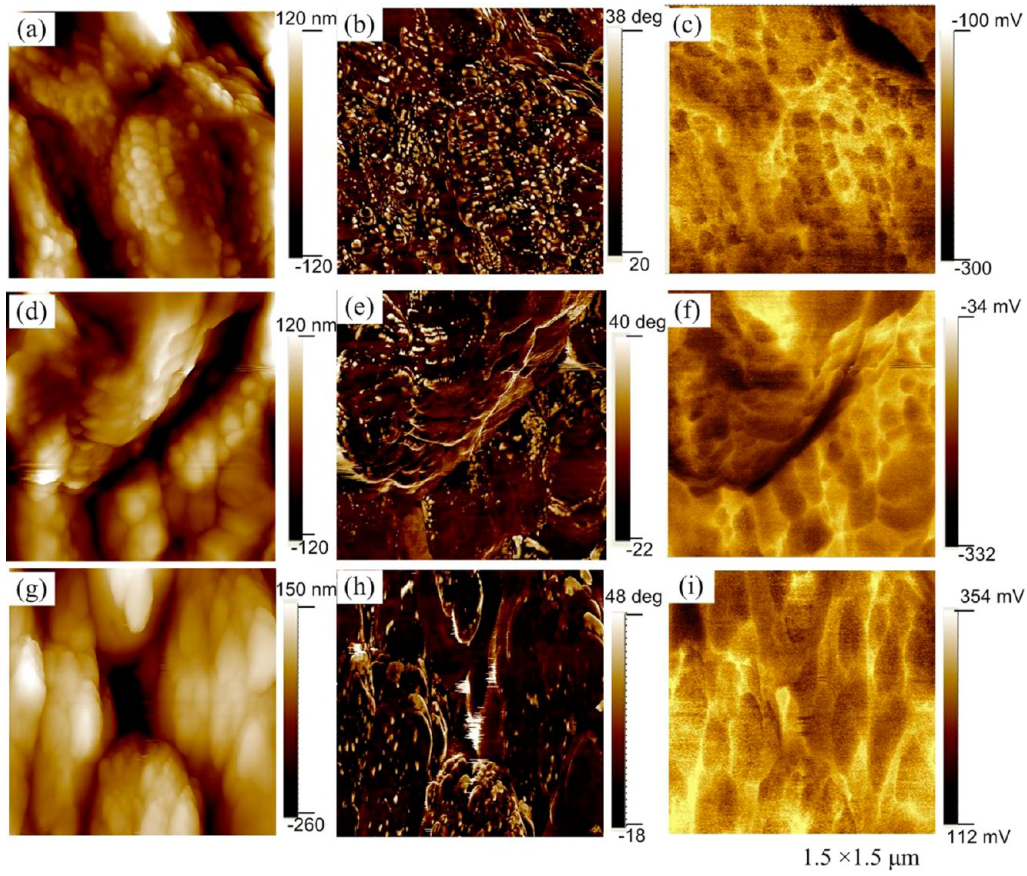

Figure 8. AFM topographic (a, d, g) , phase (b, e , h) and Volta potential (c, f, i) images of (a−c) electrodeposited Cu film [precursor: $CuSO_4$ 0.01 M, at −0.8 V for 10 min]; rGO/Cu films: (d−f) [precursor: $CuSO_4$ 0.01 M/GO 0.1 mg·mL^{-1}, at −0.8 V for 10 min] and (g−i) [precursor: $CuSO_4$ 0.01 M/GO 0.5 mg·mL^{-1}, at −1.2 V for 30 min].

potentials of these clusters are slightly smaller than their surrounding areas. The lower Volta potential of the clusters suggests that rGO sheet has slightly lower relative nobility than the surrounding (deposited Cu film). The small difference between the rGO and deposited Cu film implies a weak microgalvanic effect between the rGO sheets and the surrounding deposited Cu film, therefore a minor risk for the galvanic corrosion within the composite film.

3.4.3. EIS Analysis. The electroactivity of the deposited rGO/Cu composite films in 0.01 M NaCl solution was evaluated by the EIS measurements. The Nyquist and Bode plots are shown in Figure 9 for the polished Cu foil, electrodeposited Cu film and rGO/Cu films, respectively. In the Nyquist plot, Figure 9a, all the spectra show one semicircular arc at high frequencies, and in some cases also a straight line at low frequencies due to the Warburg impedance, i.e., the diffusion-limiting corrosion process.[65] The Bode plots of the impedance modulus, Figure 9b, and the phase angle, Figure 9c, show a certain difference between the rGO/Cu composite films and the deposited Cu film or polished Cu, and also between the rGO/Cu composite films deposited at −0.8 and −1.2 V. The low-frequency data (Warburg resistance) for the polished Cu

dx.doi.org/10.1021/am500768g | ACS Appl. Mater. Interfaces 2014, 6, 7444−7455

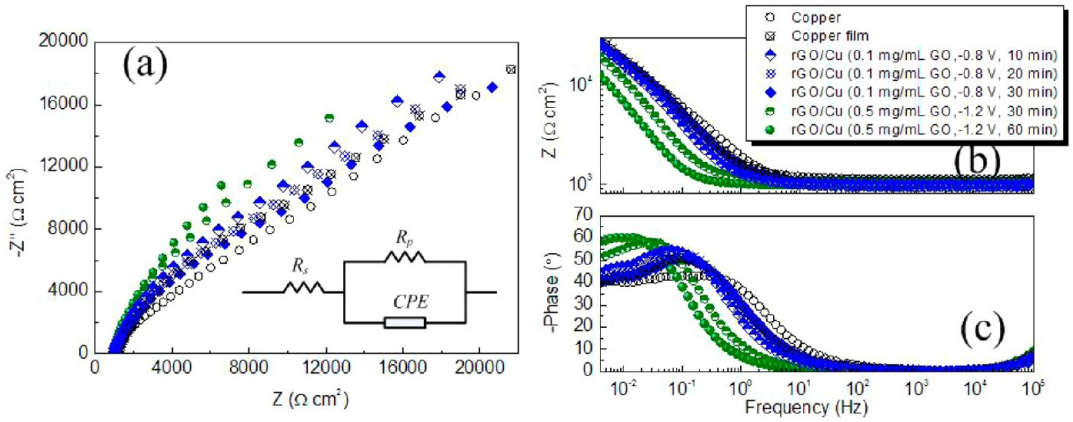

Figure 9. Nyquist (a), Bode (b) and phase (c) plots for bare Cu foil, electrodeposited Cu film and rGO/Cu films after exposure to the 0.1 M NaCl solution.

Table 4. Data Obtained from EIS Spectra Fitting

sample number	materials	R_s/kΩ cm^2	CPE/F cm^{-2} s^{n-1}	n	R_p/Ω cm^2
1	polished Cu foil	0.99 ± 0.07	(1.73 ± 0.15) × 10^{-4}	0.72	(1.90 ± 0.52) × 10^5
2	Cu film [Cu^{2+} 0.01 M (−0.8 V, 10 min)]	1.03 ± 0.07	(2.71 ± 0.3) × 10^{-4}	0.76	(3.13 ± 0.17) × 10^5
3	rGO/Cu film [Cu^{2+} 0.01 M/GO 0.1 mg·mL^{-1}, (−0.8 V, 10 min)]	1.00 ± 0.02	(4.35 ± 0.29) × 10^{-4}	0.81	(2.91 ± 0.64) × 10^5
4	rGO/Cu film [Cu^{2+} 0.01 M/GO 0.1 mg·mL^{-1}, (−0.8 V, 20 min)]	0.92 ± 0.01	(3.50 ± 0.13) × 10^{-4}	0.78	(3.00 ± 0.24) × 10^5
5	rGO/Cu film [Cu^{2+} 0.01 M/GO 0.1 mg·mL^{-1}, (−-0.8 V, 30 min)]	0.97 ± 0.03	(3.15 ± 0.47) × 10^{-4}	0.77	(2.62 ± 0.19) × 10^5
6	rGO/Cu film [Cu^{2+} 0.01 M/GO 0.5 mg·mL^{-1}, (−1.2 V, 30 min)]	1.03 ± 0.05	(7.29 ± 1.22) × 10^{-4}	0.85	(3.03 ± 0.16) × 10^5
7	rGO/Cu film [Cu^{2+} 0.01 M/GO 0.5 mg·mL^{-1}, (−1.2 V, 60 min)]	0.96 ± 0.02	(1.4 ± 0.27) × 10^{-3}	0.88	(2.88 ± 0.71) × 10^5

and deposited Cu film, i.e., Warburg impedance, indicate a diffusion-limiting corrosion process of Cu in the NaCl solution. The rGO/Cu composite films deposited at −0.8 V show a similar impedance behavior as the deposited Cu film. In contrast, the rGO/Cu composite films deposited at −1.2 V exhibit just one time−time constant, with lower impedance than the other samples. These EIS results suggest that the cathodic reduction at −1.2 V leads to the deposition of a more conducting rGO/Cu composite film, which is also stable in the NaCl solution without the sign of diffusion-limiting corrosion process.

Since the semicircle feature at high- and medium-frequency regions is associated with the resistive and capacitive properties of the metal−electrolyte interfaces, a simple equivalent electrical circuit shown in the inset of Figure 9 was used for fitting the semicircular part of the spectra, to focus on the electroactive properties of the deposited films and ignore the diffusion-related response. In the equivalent circuit, R_s is the solution resistance between the working electrode and reference electrode, R_p is the polarization resistance, i.e., charge (electron) transfer resistance, and CPE is the constant phase element for describing non-ideal capacitive response from the metal/electrolyte interface.[66] The fitting results are summarized in Table 4 (Fitting frequency range: from ~10^{-2} to 10^4 Hz). It can be seen that the rGO/Cu composite films, especially the ones deposited at −1.2 V, exhibit larger interfacial capacitances than the polished Cu foil and the electrodeposited Cu film. Considering the SEM and AFM results shown previously, and the fact that the capacitance is directly proportional to the effective surface area of the capacitor,[24] this observation can be explained by the much rougher surfaces of the hierarchical nanostructures of the composite films, which give larger electroactive surface areas at the metal−electrolyte interface. The polarization resistance (R_p) value of the polished Cu foil is the lowest, while the electrodeposited Cu filmis the highest, and the rGO/Cu films have the intermediate values. For the polished Cu, the lower R_p value is associated with the low corrosion resistance of Cu in the NaCl solution. The higher R_p of the Cu film may be due to the formation of a thin Cu_2O layer on top of the metallic Cu after the deposition and this is consistent with the electrical conductivity measurement of the samples in dry condition. The slightly higher R_p values of the rGO/Cu composite films than that of the polished Cu foil could be due to the thin Cu_2O layer formed on the surface of the deposited Cu nanograins that compose part of the composite films. For the rGO/Cu composite films, the incorporation of the more conducting rGO sheets into the composite film leads to an increased electroactivity of the surface, since the heterogeneous electron transfer capability of the rGO sheets is improved through electron mediating of Cu nanograins.[67] In other words, as compared with the electrodeposited Cu film, the rGO/Cu composite film not only increases the electrode surface area but also enhances the electron transfer at the film−electrolyte interface. It has been recently reported that rGO composite films could form thin protective layers on bare Cu foil surfaces, acting as barriers to ions transport.[60] However, for the rGO/Cu composite films in this study, the rGO sheets do not fully cover the whole surface, as demonstrated by the topographic images in Figures 3 and 8. Hence, transport of corrosive ions in the electrolyte towards the Cu substrate cannot be totally suppressed by the rGO sheets, and only the regions with rGO sheets are protected. Nevertheless, the EIS spectra of the rGO/Cu composite films deposited at −1.2 V suggest that these composite films are quite stable in the NaCl solution. In this case, the rGO sheets in the composite films maintain a good electroactivity in the electrolyte solution,[25] and meanwhile provide a certain extent of corrosion protection for the Cu substrate. As demonstrated

in Figure 8g–i, the rGO sheets are more compactly and uniformly distributed on the rGO/Cu composite film surface, which could partly act as the barrier of the ions transport. Furthermore, when the deposition time is the same (30 min), the polarization resistance of the composite film with the higher GO concentration would be slightly larger. This could be ascribed to the fact that a large amount of GO sheets inside the films would act as barriers to ion transport between the electrolytic solution and the copper substrate.

4. SUMMARY

On the basis of the results from CV, CRM, XPS, SEM, AFM/SKPFM measurements and impedance analysis, etc., the following conclusions can be drawn: By suitable preparation of the precursor solution and cathodic deposition conditions, a one-step electrochemical synthesis method can be employed to prepare rGO/Cu composite films. The CRM and SEM results suggest that copper nanograins and rGO are uniformly distributed in the deposited composite film. Due to the chelating of Cu ions by GO/rGO sheets, pine-tree-leaf nanostructures in the composite film are formed under certain electrodeposition conditions. Compared with the polished Cu foil and the electrodeposited Cu film, the rGO/Cu composite films maintain a lower electrical resistivity due to the combined effects of rGO sheets and metallic Cu grains for the enhanced transport of charge carriers in the composite film. The electrodeposited Cu film and the rGO/Cu composite films show different Volta potential variations over the surfaces. The EIS results indicate that a diffusion-limiting corrosion process may occur on the polished Cu foil and deposited Cu film in 0.01 M NaCl solution, whereas the rGO/Cu composite films deposited at −1.2 V are quite stable. The order of the electroactivity is polished Cu foil > rGO/Cu composite films > electrodeposited Cu film. The thin oxide layer on the surfaces of deposited Cu nanoparticles would weaken but the rGO sheets strengthen the electroactivity of the composite films.

AUTHOR INFORMATION

Corresponding Author

*E-mail: xgx2014@tsinghua.edu.cn, or xie-gx@163.com

Notes

The authors declare no competing financial interest.

ACKNOWLEDGMENTS

Guoxin Xie acknowledges the Ragnar Holm Postdoc Fellowship at KTH, Sweden, and the financial support from the National Natural Science Foundation of China (Grant No. 51105221). Dr. Fan Zhang at the Division of Surface and Corrosion Science at KTH is acknowledged for the discussion of the electrochemical measurements.

REFERENCES

(1) Braunovic, M.; Myshkin, N. K.; Konchits, V. V. *Electrical Contacts: Fundamentals, Applications and Technology*; CRC Press: Boca Raton, FL, 2006.

(2) Slade, P. G. *Electrical Contacts Principles and Applications*; Marcell Dekker, Inc: New York, 1999.

(3) Yang, Z.; Lichtenwalner, D. J.; Morris Jacqueline Krim, A. S.; Kingon, A. I. Comparison of Au and Au-Ni Alloys as Contact Materials for MEMS Switches. *J. Microelectromech. Syst.* **2009**, *18*, 287–295.

(4) Joshi, P. B.; Murti, N. S. S.; Gadgeel, V. L.; Kaushik, V. K.; Ramakrishnan, P. Preparation and Characterization of Ag-ZnO Powders for Applications in Electrical Contact Materials. *J. Mater. Sci. Lett.* **1995**, *14*, 1099–1101.

(5) KovZik, J.; Bielek, J. Electrical Conductivity of Cu/Graphite Composite Material as a Function of Structural Characteristics. *Scr. Mater.* **1996**, *35*, 151–156.

(6) He, D. H.; Manory, R. A Novel Electrical Contact Material with Improved Self-Lubrication for Railway Current Collectors. *Wear* **2001**, *249*, 626–636.

(7) Huang, S.; Feng, Y.; Ding, K.; Qian, G.; Liu, H.; Wang, Y. Friction and Wear Properties of Cu-Based Self-lubricating Composites in Air and Vacuum Conditions. *Acta Metall. Sin.* **2012**, *25*, 391–400.

(8) Liu, Y.; Senturk, B. S.; Mantese, J. V.; Aindow, M.; Alpay, S. P. Electrical and Tribological Properties of a Ni-18% Ru Alloy for Contact Applications. *J. Mater. Sci.* **2011**, *46*, 6563–6570.

(9) Mulligan, C. P.; Gall, D. CrN-Ag Self-lubricating Hard Coatings. *Surf. Coat. Technol.* **2005**, *200*, 1495–1500.

(10) Kutschej, K.; Mitterer, C.; Mulligan, C. P.; Gall, D. High-temperature Tribological Behavior of CrN-Ag Self-Lubricating Coatings. *Adv. Eng. Mater.* **2006**, *8*, 1125–1129.

(11) Lauridsen, J.; Eklund, P.; Jensen, J.; Ljungcrantz, H.; Öberg, Å.; Lewin, E.; Jansson, U.; Flink, A.; Högberg, H.; Hultman, L. Microstructure Evolution of Ti-Si-C-Ag Nanocomposite Coatings Deposited by DC Magnetron Sputtering. *Acta Mater.* **2010**, *58*, 6592–659.

(12) Lauridsen, J.; Eklund, P.; Lu, J.; Knutsson, A.; Oden, M.; Mannerbro, R.; Andersson, A. M.; Hultman, L. Microstructural and Chemical Analysis of AgI Coatings Used as a Solid Lubricant in Electrical Sliding Contacts. *Tribol. Lett.* **2012**, *46*, 187–193.

(13) Lu, W.; Mitchel, W. C.; Landis, G. R.; Crenshaw, T. R.; Eugene Collins, W. Electrical Contact Behavior of Ni/C60/4H-SiC Structures. *J. Vac. Sci. Technol. A* **2003**, *21*, 1510–1514.

(14) Kuchuk, A.; Kladko, V.; Adamus, Z.; Wzorek, M.; Borysiewicz, M.; Borowicz, P.; Barcz, A.; Golaszewska, K.; Piotrowska, A. Influence of Carbon Layer on the Properties of Ni-based Ohmic Contact to N-type 4H-SiC. *ISRN Electron.* **2013**, *2013*, 271658.

(15) Lei, C.; Markoulidis, F.; Ashitaka, Z.; Lekakou, C. Reduction of Porous Carbon/Al Contact Resistance for an Electric Double-Layer Capacitor (EDLC). *Electrochim. Acta* **2013**, *92*, 183–187.

(16) Park, M.; Cola, B. A.; Siegmund, T.; Xu, J.; Maschmann, M. R.; Fisher, T. S.; Kim, H. Effects of a Carbon Nanotube Layer on Electrical Contact Resistance between Copper Substrates. *Nanotechnology* **2006**, *17*, 2294–2303.

(17) Toth, G.; Maklin, J.; Halonen, N.; Palosaari, J.; Juuti, J.; Jantunen, H.; Kordas, K.; Sawyer, W. G.; Vajtai, R.; Ajayan, P. M. Carbon-Nanotube-Based Electrical Brush Contacts. *Adv. Mater.* **2009**, *21*, 1–5.

(18) Jo, G.; Choe, M.; Cho, C.; Kim, J. H.; Park, W.; Lee, S.; Hong, W.; Kim, T.; Park, S.; Hong, B. H.; Kahng, Y. H.; Lee, T. Large-Scale Patterned Multi-Layer Graphene Films as Transparent Conducting Electrodes for GaN Light-Emitting Diodes. *Nanotechnology* **2010**, *21*, 175201.

(19) Marinho, B.; Ghislandi, M.; Tkalya, E.; Koning, C. E.; de With, G. Electrical Conductivity of Compacts of Graphene, Multi-Wall Carbon Nanotubes, Carbon Black, and Graphite Powder. *Powder Technol.* **2012**, *221*, 351–358.

(20) Balandin, A. A.; Ghosh, S.; Bao, W.; Calizo, I.; Teweldebrhan, D.; Miao, F.; Lau, C. N. Superior Thermal Conductivity of Single-Layer Graphene. *Nano Lett.* **2008**, *8*, 902–907.

(21) Scarpa, F.; Adhikari, S.; Srikantha Phani, A. Effective Elastic Mechanical Properties of Single Layer Graphene Sheets. *Nanotechnology* **2009**, *20*, 065709.

(22) Berman, D.; Erdemir, A.; Sumant, A. V. Reduced Wear and Friction Enabled by Graphene Layers on Sliding Steel Surfaces in Dry Nitrogen. *Carbon* **2013**, *59*, 167–175.

(23) Kirkland, N.T.; Schiller, T.; Medhekar, N.; Birbilis, N. Exploring Graphene as a Corrosion Protection Barrier. *Corros. Sci.* **2012**, *56*, 1–4.

(24) Singh Raman, R.K.; Chakraborty Banerjee, P.; Lobo, D. E.; Gullapalli, H.; Sumandasa, M.; Kumar, A.; Choudhary, L.; Tkacz, R.;

Ajayan, P. M.; Majumder, M. Protecting Copper from Electrochemical Degradation by Graphene Coating. *Carbon* **2012**, *50*, 4040−4045.
(25) Schriver, M.; Regan, W.; Gannett, W. J.; Zaniewski, A. M.; Crommie, M. F.; Zett, A. Graphene as a Long-term Metal Oxidation Barrier: Worse than Nothing. *ACS Nano* **2013**, *7*, 5763−5768.
(26) Wang, B.; Wu, X.; Shu, C.; Guo, Y.; Wang, C. Synthesis of CuO/Graphene Nanocomposite as a High-performance Anode Material for Lithium-ion Batteries. *J. Mater. Chem.* **2010**, *20*, 10661−10664.
(27) Gao, R.; Hu, N.; Yang, Z.; Zhu, Q.; Chai, J.; Su, Y.; Zhang, L.; Zhang, Y. Paper-Like Graphene-Ag Composite Films with Enhanced Mechanical and Electrical Properties. *Nanoscale Res. Lett.* **2013**, *8*, 32.
(28) Zhong, C.; Wang, J.; Gao, X.; Wexler, D.; Liu, H. In Situ One-step Synthesis of a 3D Nanostructured Germanium-Graphene Composite and Its Application in Lithium-Ion Batteries. *J. Mater. Chem. A* **2013**, *1*, 10798.
(29) Wu, S.; Yin, Z.; He, Q.; Huang, X.; Zhou, X.; Zhang, H. Electrochemical Deposition of Semiconductor Oxides on Reduced Graphene Oxide-Based Flexible, Transparent, and Conductive Electrodes. *J. Phys. Chem. C* **2010**, *114*, 11816−11821.
(30) Kholmanov, I. N.; Domingues, S. H.; Chou, H.; Wang, X.; Tan, C.; Kim, J.; Li, H.; Piner, R.; Zarbin, A. J. G.; Ruoff, R. S. Reduced Graphene Oxide/copper Nanowire Hybrid Films as High-Performance Transparent Electrodes. *ACS Nano* **2013**, *7*, 1811−1816.
(31) Mai, Y.J.; Wang, X.L.; Xiang, J.Y.; Qiao, Y.Q.; Zhang, D.; Gu, C.D.; Tu, J.P. CuO/Graphene Composite as Anode Materials for Lithium-Ion Batteries. *Electrochim. Acta* **2011**, *56*, 2306−2311.
(32) Perret, P. G.; Malenfant, P. R. L.; Bock, C.; MacDougall, B. Electro-deposition and Dissolution of MnO_2 on a Graphene Composite Electrode for Its Utilization in an Aqueous Based Hybrid Supercapacitor. *J. Electrochem. Soc.* **2012**, *159*, A1554−A1561.
(33) Hilder, M.; Winther-Jensen, O.; Winther-Jensen, B.; MacFarlane, D. R. Graphene/Zinc Nano-composites by Electrochemical Co-deposition. *Phys. Chem. Chem. Phys.* **2012**, *14*, 14034−14040.
(34) Kim, G.; Nam, I.; Kim, N. D.; Park, J.; Park, S.; Yi, J. A Synthesis of Graphene/Co_3O_4 Thin Films for Lithium Ion Battery Anodes by Coelectrodeposition. *Electrochem. Commun.* **2012**, *22*, 93−96.
(35) Jagannadham, K. Electrical Conductivity of Copper-Graphene Composite Films Synthesized by Electrochemical Deposition with Exfoliated Graphene Platelets. *J. Vac. Sci. Technol. B* **2012**, *30*, 03D109.
(36) Jagannadham, K. Volume Fraction of Graphene Platelets in Copper-Graphene Composites. *Metall. Mater. Trans. A* **2013**, *44*, 552−559.
(37) Zhang, Y.; Liu, S.; Wang, L.; Qin, X.; Tian, J.; Lu, W.; Chang, G.; Sun, X. One-pot Green Synthesis of Ag Nanoparticles-Graphene Nanocomposites and Their Applications in SERS, H_2O_2, and Glucose Sensing. *RSC Adv.* **2012**, *2*, 538−545.
(38) Du, D.; Liu, J.; Zhang, X.; Cui, X.; Lin, Y. One-step Electrochemical Deposition of a Graphene-ZrO_2 Nanocomposite: Preparation, Characterization and Application for Detection of Organophosphorus Agents. *J. Mater. Chem.* **2011**, *21*, 8032.
(39) Zhuo, Q.; Ma, Y.; Gao, J.; Zhang, P.; Xia, Y.; Tian, Y.; Sun, X.; Zhong, J.; Sun, X. Facile Synthesis of Graphene/Metal Nanoparticle Composites via Self-catalysis Reduction at Room Temperature. *Inorg. Chem.* **2013**, *52*, 3141−3147.
(40) Tran, P. D.; Batabyal, S. K.; Pramana, S. S.; Barber, J.; Wong, L. H.; Loo, S. C. J. A Cuprous Oxide-Reduced Graphene Oxide (Cu_2O-rGO) Composite Photocatalyst for Hydrogen Generation: Employing RGO as an Electron Acceptor to Enhance the Photocatalytic Activity and Stability of Cu_2O. *Nanoscale* **2012**, *4*, 3875.
(41) Kim, Y.; Lee, J.; Yeom, M. S.; Shi, J. W.; Kim, H.; Cui, Y.; Kysar, J. W.; Hone, J.; Jung, Y.; Jeon, S.; Han, S. M. Strengthening Effect of Single-atomic-layer Graphene in Metal-Graphene Nanolayered Composites. *Nat. Commun.* **2013**, *4*, 2114.
(42) Tu, Q.; Pang, L.; Chen, Y.; Zhang, Y.; Zhang, R.; Lu, B.; Wang, J. Effects of Surface Charges of Graphene Oxide on Neuronal Outgrowth and Branching. *Analyst* **2014**, *139*, 105−115.
(43) Hilder, M.; Winther-Jensen, B.; Li, D.; Forsyth, M.; MacFarlane, D. R. Direct Electro-deposition of Graphene from Aqueous Suspensions. *Phys. Chem. Chem. Phys.* **2011**, *13*, 9187−9193.
(44) Liu, C.; Wang, K.; Luo, S.; Tang, Y.; Chen, L. Direct Electrodeposition of Graphene Enabling the One-step Synthesis of Graphene-metal Nanocomposite Films. *Small* **2011**, *7*, 1203−1206.
(45) Forslund, M.; Leygraf, C.; Claesson, P. M.; Lin, C.; Pan, J. Micro-galvanic Corrosion Effects on Patterned Copper-zinc Samples during Exposure in Humidified Air Containing Formic Acid. *J. Electrochem. Soc.* **2013**, *160*, C423−C431.
(46) Guillaumin, V.; Schmutz, P.; Frankel, G.S. Characterization of Corrosion Interfaces by the Scanning Kelvin Probe Force Microscopy Technique. *J. Electrochem. Soc.* **2001**, *148*, B163−B173.
(47) Sitko, R.; Turek, E.; Zawisza, B.; Malicka, E.; Talik, E.; Heimann, J.; Gagor, A.; Feist, B.; Wrzali, R. Adsorption of Divalent Metal Ions from Aqueous Solutions using Graphene Oxide. *Dalton Trans.* **2013**, *42*, 5682−5689.
(48) Wu, Z.; Yau, S. Examination of Underpotential Deposition of Copper on Pt (111) Electrodes in Hydrochloric Acid Solutions with In Situ Scanning Tunneling Microscopy. *Langmuir* **2001**, *17*, 4627−4633.
(49) Grujicic, D.; Pesic, B. Electrodeposition of Copper: the Nucleation Mechanisms. *Electrochim. Acta* **2012**, *47*, 2901−2912.
(50) Shao, Y.; Wang, J.; Engelhard, M.; Wang, C.; Lin, Y. Facile and Controllable Electrochemical Reduction of Graphene Oxide and Its Applications. *J. Mater. Chem.* **2010**, *20*, 743−748.
(51) Li, Z.; Zhang, H.; Ge, X.; Liang, Y.; An, X.; Yang, C.; Fang, B.; Xie, H.; Wei, J. A Nanocomposite of Copper(II) Functionalized Graphene and Application for Sensing Sulfurated Organophosphorus Pesticides. *New J. Chem.* **2013**, *37*, 3956.
(52) Zhang, X.; Zhang, D.; Chen, Y.; Sun, X.; Ma, Y. Electrochemical Reduction of Graphene Oxide Films: Preparation, Characterization and Their Electrochemical Properties. *Chin. Sci. Bull.* **2012**, *57*, 3045−3050.
(53) Cerisiera, M.; Attenborougha, K.; Fransaera, J.; Van Haesendonckb, C.; Celisa, J. P. Growth Mode of Copper Films Electrodeposited on Silicon From Sulfate and Pyrophosphate Solutions. *J. Electrochem. Soc.* **1999**, *146*, 2156−2162.
(54) Liu, Z.; Ding, L.; Wang, Z.; Mao, Y.; Xie, S.; Zhang, Y.; Li, G.; Tong, Y. ZnO/SnO_2 Hierarchical and Flower-like Nanostructures: Facile Synthesis, Formation Mechanism, and Optical and Magnetic Properties. *CrystEngComm* **2012**, *14*, 2289.
(55) Li, C.; Zeng, H. Cobalt (hcp) Nanofibers with Pine-tree-leaf Hierarchical Superstructures. *J. Mater. Chem.* **2010**, *20*, 9187−9192.
(56) Zhang, J.; Yan, B.; Zhang, F. Synthesis of Carbon-coated Fe_3O_4 Composites with Pine-tree-leaf Structures from Catalytic Pyrolysis of Polyethylene. *CrystEngComm* **2012**, *14*, 3451.
(57) Yang, J.; Duan, X.; Qin, Q.; Zheng, W. Solvothermal Synthesis of Hierarchical Flower-like β-NiS with Excellent Electrochemical Performance for Supercapacitors. *J. Mater. Chem. A* **2013**, *1*, 7880.
(58) Malard, L.M.; Pimenta, M.A.; Dresselhaus, G.; Dresselhaus, M.S. Raman Spectroscopy in Graphene. *Phys. Rep.* **2009**, *473*, 51−87.
(59) Liu, H.; Zhang, L.; Guo, Y.; Cheng, C.; Yang, L.; Jiang, L.; Yu, G.; Hu, W.; Liu, Y.; Zhu, D. Reduction of Graphene Oxide to Highly Conductive Graphene by Lawesson's Reagent and Its Electrical Applications. *J. Mater. Chem. C* **2013**, *1*, 3104−3109.
(60) Singh, B. P.; Nayak, S.; Nanda, K. K.; Jena, B. K.; Bhattacharjee, S.; Besra, L. The Production of a Corrosion Resistant Graphene Reinforced Composite Coating on Copper by Electrophoretic Deposition. *Carbon* **2013**, *61*, 47−56.
(61) Zhao, Y.; Song, X.; Song, Q.; Yin, Z. A Facile Route to the Synthesis Copper Oxide/Reduced Graphene Oxide Nanocomposites and Electrochemical Detection of Catechol Organic Pollutant. *CrystEngComm* **2012**, *14*, 6710−6719.
(62) Hurley, B. L.; Qiu, S.; Buchheit, R. G. Raman Spectroscopy Characterization of Aqueous Vanadate Species Interaction with Aluminum Alloy 2024-T3 Surfaces. *J. Electrochem. Soc.* **2011**, *158*, C125−C131.

(63) Cano, E.; Torres, C. L.; Bastidas, J. M. An XPS Study of Copper Corrosion Originated by Formic Acid Vapour at 40% and 80% Relative Humidity. *Mater. Corros.* **2001**, *52*, 667−676.
(64) Waechtler, T.; Oswald, S.; Roth, N.; Jakob, A.; Lang, H.; Schulz, R. E. E.; Gessner, T.; Moskvinova, A.; Schulze, S.; Hietschold, M. Copper Oxide Films Grown by Atomic Layer Deposition from Bis(tri-n-butylphosphane)copper(I)acetylacetonate on Ta, TaN, Ru, and SiO_2. *J. Electrochem. Soc.* **2009**, *156*, H453−H459.
(65) Ye, J.; Cui, H.; Liu, X.; Lim, T.; Zhang, W.; Sheu, F. Preparation and Characterization of Aligned Carbon Nanotube-Ruthenium Oxide Nanocomposites for Supercapacitors. *Small* **2005**, *1*, 560−565.
(66) Zhang, F.; Pan, J.; Lin, C. Localized Corrosion Behaviour of Reinforcement Steel in Simulated Concrete Pore Solution. *Corros. Sci.* **2009**, *51*, 2130−2138.
(67) Luo, J.; Jiang, S.; Zhang, H.; Jiang, J.; Liu, X. A Novel Non-enzymatic Glucose Sensor Based on Cu Nanoparticle Modified Graphene Sheets Electrode. *Anal. Chim. Acta* **2012**, *709*, 47−53.